nature communications

Article

https://doi.org/10.1038/s41467-024-52022-0

Stabilized Cu^0 -Cu^{1+} dual sites in a cyanamide framework for selective CO_2 electroreduction to ethylene

Received: 7 February 2024

Accepted: 22 August 2024

Published online: 07 September 2024

Check for updates

Kaihang Yue[1,2,6], Yanyang Qin[3,6], Honghao Huang[1], Zhuoran Lv[1,4], Mingzhi Cai[4,5], Yaqiong Su[3] ✉, Fuqiang Huang[1,4] ✉ & Ya Yan[1,2] ✉

Electrochemical reduction of carbon dioxide to produce high-value ethylene is often limited by poor selectivity and yield of multi-carbon products. To address this, we propose a cyanamide-coordinated isolated copper framework with both metallic copper (Cu^0) and charged copper (Cu^{1+}) sites as an efficient electrocatalyst for the reduction of carbon dioxide to ethylene. Our *operando* electrochemical characterizations and theoretical calculations reveal that copper atoms in the $Cu^{\delta+}$NCN complex enhance carbon dioxide activation by improving surface carbon monoxide adsorption, while delocalized electrons around copper sites facilitate carbon-carbon coupling by reducing the Gibbs free energy for *CHC formation. This leads to high selectivity for ethylene production. The $Cu^{\delta+}$NCN catalyst achieves 77.7% selectivity for carbon dioxide to ethylene conversion at a partial current density of 400 milliamperes per square centimeter and demonstrates long-term stability over 80 hours in membrane electrode assembly-based electrolysers. This study provides a strategic approach for designing catalysts for the electrosynthesis of value-added chemicals from carbon dioxide.

Carbon conversion via electrochemical CO_2 reduction reaction (CO_2RR) provides a promising solution to mitigate rising CO_2 levels and simultaneously production of fuels and value-added feedstocks[1–3]. Relative to the research on C_1 products, higher C_2 hydrocarbons, such as ethylene (C_2H_4), is a more high-value-added product but suffer from difficulty of effective C–C coupling in CO_2RR process[4–6]. A key challenge facing the current CO_2RR electrocatalyst is how to improve energy efficiency by enhancing a single-product Faradaic efficiency (FE) with low overpotentials while keeping the catalyst durability at elevating current density[7,8]. Among various electrocatalysts, copper oxidation states preserved materials are known to be the most effective for CO_2-to-C_2H_4 conversion. However, the self-reduction and undesirable reconstruction makes these copper-based catalysts offering limited activity and selectivity to the desirable C_2H_4 production[9,10].

Recently, it has been revealed that manipulating oxidation states to achieve the well balance of Cu^0 and Cu^{1+} during CO_2RR is vital for CO_2-to-C_2H_4[11–13]. It is found the Cu^0 site can activate CO_2 and facilitate the following electron transfers, while the Cu^{1+} site strengthens the adsorption of adsorbed CO (*CO) and boosts C–C coupling to afford effective production of C_2H_4[14–16]. Several representative reports constructing reversible transformation process to stabilize the Cu^0-Cu^{1+} ensembles on the designed copper oxides, or the support assisted copper oxides (Fig. 1a, i)[17–19]. However, the C_2 conversion mostly

[1]State Key Laboratory of High Performance Ceramics and Superfine Microstructure, Shanghai Institute of Ceramics, Chinese Academy of Sciences, Shanghai 200050, China. [2]Center of Materials Science and Optoelectronics Engineering, University of Chinese Academy of Sciences, Beijing 100049, China. [3]School of Chemistry, Xi'an Jiaotong University, Xi'an 710049, China. [4]State Key Lab of Metal Matrix Composites, School of Materials Science and Engineering, Shanghai Jiao Tong University, Shanghai 200240, China. [5]State Key Laboratory of Rare Earth Materials Chemistry and Applications College of Chemistry and Molecular Engineering, Peking University, Beijing 100871, China. [6]These authors contributed equally: Kaihang Yue, Yanyang Qin. ✉e-mail: yqsu1989@xjtu.edu.cn; huangfq@sjtu.edu.cn; yanya@mail.sic.ac.cn

limited at small potential window as the catalysts would behave copper-like CO_2RR performance at a higher cathodic potential. Although constructing synergistic Cu^0-Cu^{1+} interfaces via Cu-based heterogeneous (*e.g.* Cu/Cu_xS_x, Cu/CuPO) materials can increase the current density of CO_2RR and achieve a highly selective, but instability currently happens due to the solubility of polysulfide or polyphosphate, during long-term high redox potentials (Fig. 1a, ii)[20–22].

Inspired by the strengths and weaknesses of these strategies, finely coordinating Cu^0-Cu^{1+} ensembles with $[NCN]^{2-}$ group to form multi-atom ion-composed compounds different from oxides and chalcogenides will maximize the potential of such models and thus achieve the co-existence of Cu^0 and Cu^{1+} dual sites in the framework, where the isolated Cu^0 can strongly conjugate with the Cu−N in Cu_2NCN (Fig. 1a, iii). The advantage of such structure lies in the cyanamide anions $[NCN]^{2-}$, on one hand, is a strongly σ-donating ligand can delocalize Cu *d*-electrons, on the other hand, π electrons flowing among $[N{-}C{\equiv}N]^{2-}$ or $[N{\equiv}C{-}N]^{2-}$ or $[N{=}C{=}N]^{2-}$ bonds would potentially improve electrons conductivity and thus prevent the Cu^+ from self-reduction[23–25]. Moreover, the spacious crystal structure resulted from parallel aligned $[NCN]^{2-}$ would maximum exposure of the active sites and brings about abundant channel for the adsorption of reagents.

Focusing on this vision, we herein proposed an isolated metallic Cu atom conjugated Cu_2NCN framework (donated as $Cu^{\delta+}NCN$) by the structure cleavage of CuNCN to trigger a phase transition via a stepwise reduction strategy, which worked as a robust catalytic model to stabilize the copper oxidation state for high CO_2RR activity and selectivity for C_2H_4. Specifically, aberration-corrected transmission electron microscope (AC-TEM), synchrotron-based X-ray absorption near-edge structure (XANES) spectroscopy and extended X-ray absorption fine structure (EXAFS) studies consistently confirmed that the linear $[NCN]^{2-}$ anions in the $Cu^{\delta+}NCN$ open framework stabilize the Cu^0-Cu^{1+} ensembles by strong covalent interactions and the fast electrons transfer nature, which afforded the highly active $Cu^{\delta+}$ species maintaining well balance of Cu^0-Cu^{1+} dual sites rather than the evolution of self-reduced Cu^0 metal during the CO_2RR. Furthermore, combined results of *operando* X-ray absorption spectroscopy (XAS), *operando* attenuated total reflection-surface enhanced infrared absorption spectroscopy (ATR-SEIRA) and density functional theory (DFT) simulation, the synergetic effect of isolated Cu^0 sites and positively charged Cu^{1+} was elucidated that the Cu^0 sites can adsorb and activate the CO_2 while the neighboring Cu^{1+} sites accelerated the C−C coupling and enabled a highly selective conversion of CO_2 to C_2H_4. Benefitting from the $[NCN]^{2-}$ open framework stabilized Cu^0-Cu^{1+} ensembles, $Cu^{\delta+}NCN$ exhibited an exceptional catalytic selectivity featuring a C_2H_4 Faradaic efficiency higher than 75% at 400 mA cm^{-2} over a 15 h constant CO_2RR. Significantly, such rationally designed active sites/conductive group coordinated open framework could provide valuable insights for the development of highly selective and stable CO_2RR catalysts for the electrosynthesis of higher-value products.

Results and discussion

Structural characterizations of $Cu^{\delta+}NCN$

A conventional CuNCN prepared from a liquid-phase precipitation was chemically cleaved by hydrazine acting as reduction agent to fabricate the $Cu^{\delta+}NCN$ structure composed of soft Cu (Cu^{1+}) and hard Cu (Cu^0) dual sites that stabilized by $[NCN]^{2-}$ group (Methods in Supporting Information). The X-ray diffraction (XRD) pattern of $Cu^{\delta+}NCN$ displayed a monoclinic phase that similar to the Cu_2NCN (Fig. 1b). For comparison, CuNCN and CuO nanostructures were also synthesized with similar method (Fig. 2a and Supplementary Figs. 1, 2). Scanning electronic microscopy (SEM) image revealed the as-prepared $Cu^{\delta+}NCN$ display a morphology of assembled nanosheets (Fig. 1c), this is further verified by transmission electron microscopy (TEM) characterization, where well-defined nanosheet with a thickness of 14 nm was observed (Fig. 1d, Supplementary Fig. 3). Significant polycrystalline diffraction signals appear on the (001), (021) and (020) faces of the monoclinic $Cu^{\delta+}NCN$ in the Fast Fourier transform (FFT) map of the [001] region (Fig. 1e).The high-angle annular bright-field (HAABF) images of scanning transmission electron microscope (STEM) along the [001] zone indicated that the local atomic distribution and crystal structure were consistent with monoclinic Cu_2NCN (Fig. 1f; Supplementary Fig 4). Additionally, the energy dispersive spectroscopy (EDS) mapping analysis of $Cu^{\delta+}NCN$ pointed out the uniform distribution of Cu, N and C elements throughout the nanosheet (Fig. 1g). The elemental content of Cu was confirmed to be 67.23% by Inductively Coupled Plasma Optical Emission Spectrometry (ICP-OES), in comparison to the 60.45% in CuNCN, this can be attributed to the reduction by hydrazine hydrate leading to a decrease in the $[NCN]^{2-}$ group ratio. (Supplementary Table 1).

X-ray photoelectron spectroscopy (XPS) was conducted to investigate the surface composition and chemical states of $Cu^{\delta+}NCN$ (Supplementary Fig. 5). From the deconvoluted Cu 2*p* spectra, two peaks centered at 932.80 and 952.68 eV were assigned to $2p_{3/2}$ and $2p_{1/2}$ of Cu^0 or Cu^{1+} species, respectively (Supplementary Fig. 5b). Auger emission spectrum (AES) of Cu LMM further suggested the coexistence of Cu^0 and Cu^{1+} in $Cu^{\delta+}NCN$ (Fig. 2a). Then, X-ray absorption spectroscopy (XAS) was performed to analyze the electronic structure and local coordination environment of Cu in $Cu^{\delta+}NCN$. The X-ray absorption near edge structure (XANES) spectra together with the first-order derivative revealed the valence state of Cu in $Cu^{\delta+}NCN$ is located between Cu^{1+} and Cu^0 (Fig. 2b, c)[26]. The Fourier transform k^3-weighted Cu K-edge extended X-ray absorption fine structure (EXAFS) spectra revealed that both Cu−N region (with a distance of ~1.5 Å) and Cu−Cu region (with a distance of 2.18 Å) were observed in $Cu^{\delta+}NCN$ (Fig. 2d). The Cu−N/C/O coordination number (CN) of $Cu^{\delta+}NCN$ was confirmed to be 1.6, smaller than that of Cu_2NCN (CN = 2) in the first coordination layer by fitting the EXAFS spectra (Supplementary Tables 2, 3). By integrating the structural information observed from $Cu^{\delta+}NCN$: the Cu−N/C/O coordination number in EXAFS being less than the theoretical value, the average valence state residing between 0 and +1 in the XAS K-edge, and the presence of both Cu^0 and Cu^{1+} atoms indicated by the Cu LMM Auger spectrum, we can deduce that both Cu^0 and Cu^{1+} coexist on the surface of $Cu^{\delta+}NCN$. To evaluate the charge states at the $Cu^{\delta+}NCN$, the distribution of surface electrostatic potential was measured by using Kelvin probe force microscopy (KPFM) in atomic force microscopy (AFM). Figure 2e and Supplementary Fig. 3 showed the respective surface electrostatic potential maps and the intensity profiles across the samples, where the intensities correspond to the relative surface potentials and a smaller surface electrostatic potential would endow the catalyst good CO_2 adsorption and electron transfer ability[27]. As observed, the surface electrostatic potential of $Cu^{\delta+}NCN$ was distinctly lower compared with the CuNCN and CuO, suggesting the favorable charge states for CO_2RR. Moreover, the coordination mode of Cu with $[NCN]^{2-}$ group in $Cu^{\delta+}NCN$ was analyzed by Fourier-transform infrared spectroscopy (FTIR), and the characteristic vibration peaks clearly proved that the $[N{-}C{\equiv}N]^{2-}$ and $[N{=}C{=}N]^{2-}$ coexisted in $Cu^{\delta+}NCN$, which was different from CuNCN, only $[N{=}C{=}N]^{2-}$ can be observed (Fig. 2f). As revealed by our previous work, $[N{-}C{\equiv}N]^{2-}$ anions prefers to bind to softer cations (e.g. Cu^{1+}) to create an electron delocalization of the Cu atoms in the framework[24]. In addition, the favorable proton and electron transfer nature of $[NCN]^{2-}$ can accelerate the CO_2RR. Consequently, the aforementioned results allow the reasonable structural determination of the $Cu^{\delta+}NCN$ nanosheets with coexisted isolated Cu^0-Cu^{1+} dual sites along with prime charge transfer characteristic.

https://doi.org/10.1038/s41467-024-52022-0

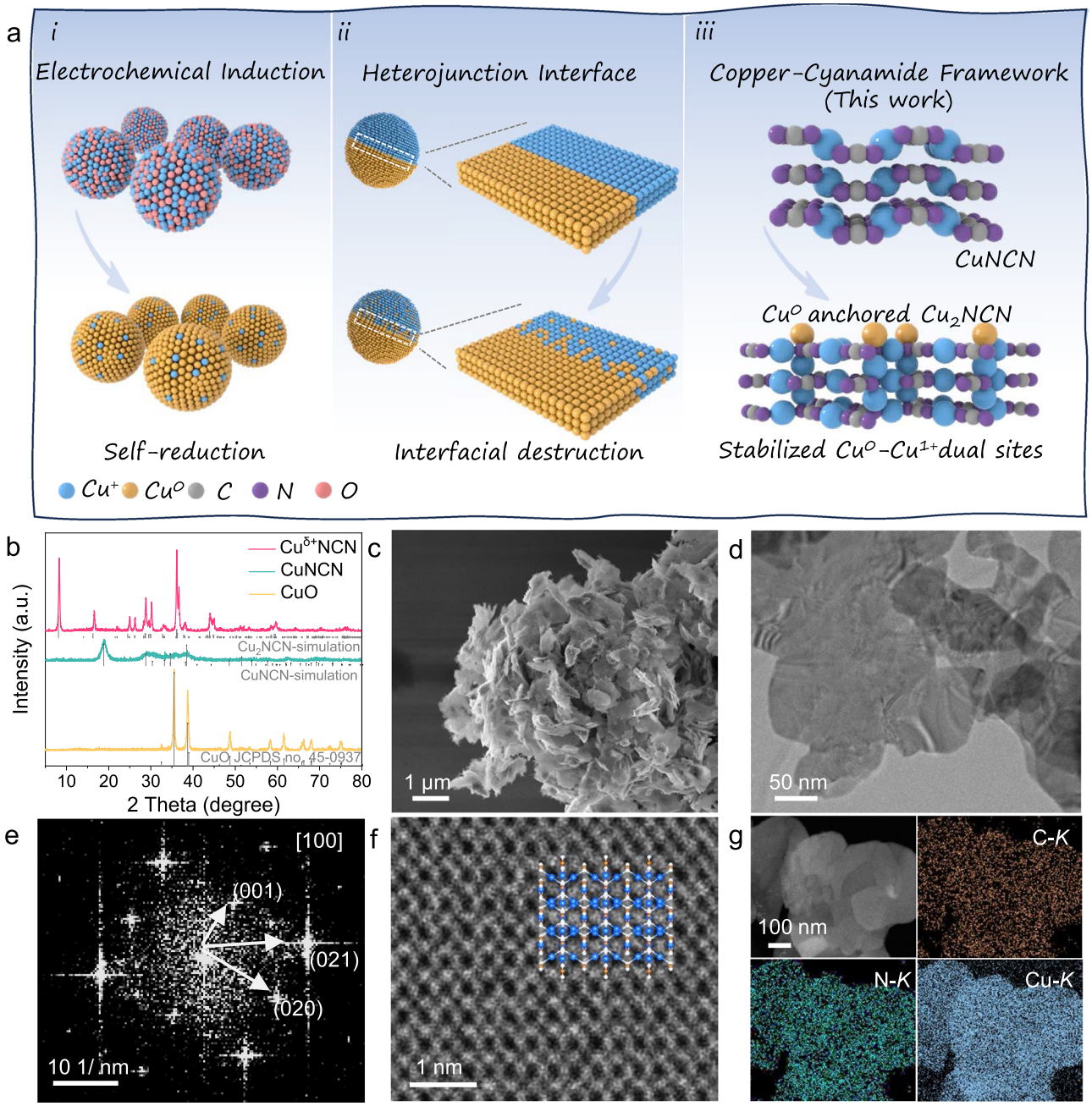

Fig. 1 | Design scheme and structural characterizations. a Schematic illustration of the construction of Cu^0-Cu^{1+} catalytic sites: (i) Electrochemical induction. (ii) Heterojunction interface. (iii) Stabilized Cu^0-Cu^{1+} dual sites via cyanamide framework (this work). **b** XRD patterns of $Cu^{\delta+}$NCN, CuNCN and CuO. **c** SEM and (**d**) TEM images of $Cu^{\delta+}$NCN. **e** FFT diagrams of of $Cu^{\delta+}$NCN. **f** Aberration-corrected HAABF-STEM images of $Cu^{\delta+}$NCN along the [001] zone. **g** EDS mapping of $Cu^{\delta+}$NCN.

CO_2 electroreduction performances

The electrochemical CO_2RR experiments on $Cu^{\delta+}$NCN were firstly evaluated in CO_2-saturated 1.0 M KOH solution in a flow cell. Linear scanning voltammetry (LSV) curves (Fig. 3a) showed that $Cu^{\delta+}$NCN exhibited the lowest onset potentials as well as better reaction kinetics, especially in the presence of CO_2, compared to CuNCN and CuO. Figure 3b showed the product selectivity of CO_2RR on $Cu^{\delta+}$NCN and contrast samples, and the electroreduction products were quantified by both gas chromatography and Nuclear Magnetic Resonance (NMR) spectroscopy (Supplementary Fig. 6). $Cu^{\delta+}$NCN showed a prominent selectivity for C_2H_4 (FE_{C2H4} > 50%) over the whole measured potentials from −1.0 to −1.6 V vs. RHE, it peaked at −1.4 V with a FE_{C2H4} of 72.6 ± 5.1% (Fig. 3b), corresponding to a partial current density for C_2H_4 (j_{C2H4}) of almost −400 mA cm^{-2} (Fig. 3c). As a comparison, the CuNCN and CuO were less selective and its CO_2RR catalysis yielded almost an equal amount of C_1 and C_2 products along with FE_{C2H4} in the range of 20-40% (Fig. 3b). It is important to note that although the total catalytic current density of $Cu^{\delta+}$NCN is lower than that of CuO in the range of −1.0 V to −1.3 V vs RHE, the j_{C2H4} on $Cu^{\delta+}$NCN is significantly more advantageous due to its high FE_{C2H4}, and this advantage becomes even more pronounced as the potential increases (Fig. 3c). Thereafter, a chronoamperometry study on $Cu^{\delta+}$NCN catalyst over a 15 h span at −1.4 V vs. RHE showed an excellent stability in both current density (~ 400 mA cm^{-2}) and FE (~70%) of CO_2-to-C_2H_4 (Fig. 3d) In contrast, the FE_{C2H4} of CuNCN decreased from ~40% to ~18% after only 2 h under the same conditions (Supplementary Fig. 7). By comparing the

https://doi.org/10.1038/s41467-024-52022-0

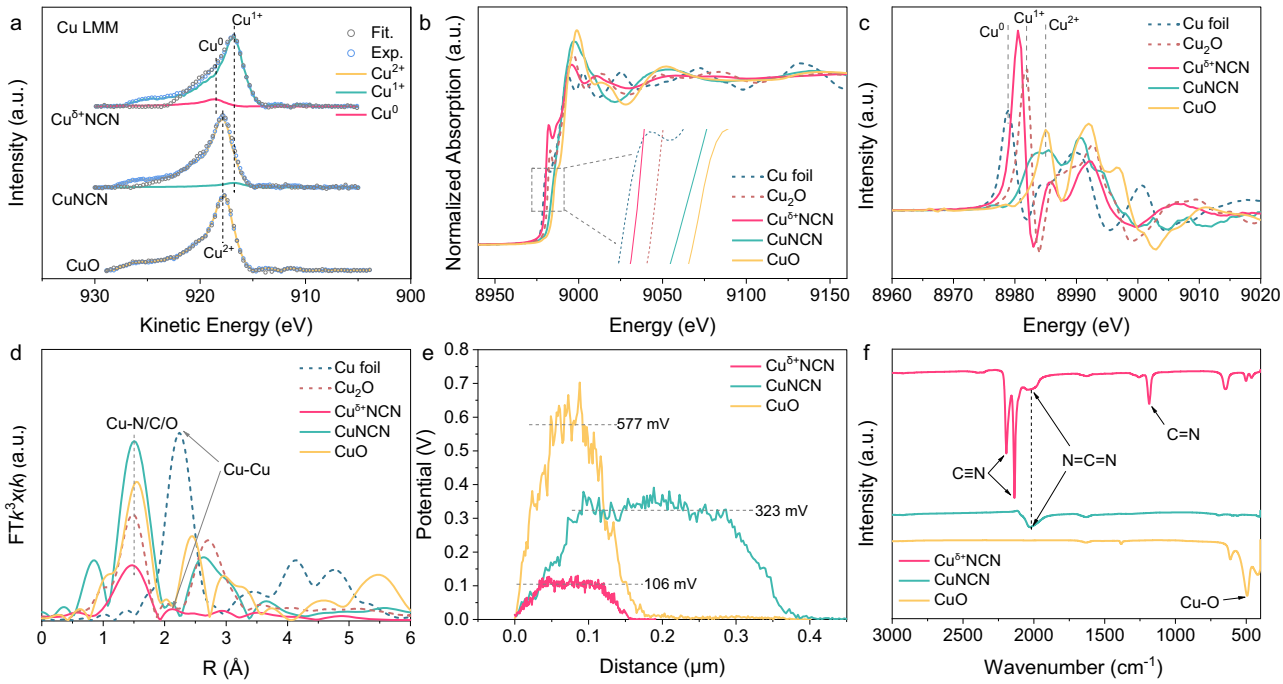

Fig. 2 | Electronic and fine structural characterizations. a Cu LMM spectra of $Cu^{\delta+}$NCN, CuNCN and CuO. **b** Normalized Cu K-edge XANES spectra and **c** the derived normalized $\chi\mu(E)$ spectra of $Cu^{\delta+}$NCN, CuNCN, CuO, Cu foil and standard Cu_2O samples. **d** FT-EXAFS spectra of $Cu^{\delta+}$NCN, CuNCN, CuO, Cu foil and standard Cu_2O samples. **e** Surface potential profiles of $Cu^{\delta+}$NCN, CuNCN and CuO. **f** FT-IR spectra of $Cu^{\delta+}$NCN, CuNCN and CuO.

FE of CO_2 to C_2H_4 and corresponding *j* of $Cu^{\delta+}$NCN with that for other reported excellent Cu-based electrocatalysts (Fig. 3e and Supplementary Tab. 4), the CO_2RR performance of $Cu^{\delta+}$NCN was found to locate in the best ranks of these Cu-based materials[8,14,17–19,28–34].

Subsequently, we studied the CO_2RR catalysis over $Cu^{\delta+}$NCN catalysts prepared with different reduction degree (Supplementary Fig. 8). For each catalyst, the FE and product distribution of each catalyst were measured, and the sample obtained with 5 mL of hydrazine displayed highest FE for C_2H_4 (Fig. 3b). In addition, we explored the hydrophilic and hydrophilic properties by contact angle measurements, and the electrochemical surface areas (ECSA) were also evaluated by the double-layer capacitance method: $Cu^{\delta+}$NCN, CuNCN and CuO displayed similar hydrophilic ability and ECSA (Supplementary Fig. 9&10), suggesting that the hydrophobicity and surface area are not major contributors to the differences in the CO_2RR performance.

Furthermore, the electrocatalytic CO_2 reduction of the $Cu^{\delta+}$NCN catalyst was implemented in an anion-exchange membrane (AEM) + proton-exchange membrane (PEM) assembled membrane electrode assembly (MEA) system[35], where the pure H_2O was supplied as the anolyte to suppress carbonate formation and precipitation, as well as to diminish the solution resistance inherent in traditional flow cell (Fig. 3f). The double membrane-based MEA electrolyzer heralds a substantial enhancement in electrocatalytic efficacy and current output for the reduction of CO_2, culminating in a remarkable current density of 180 mA cm^{-2} at a cell voltage of 3.6 V (Fig. 3g). Of particular note, this configuration sustains a high FE of 66.8% for the electrosynthesis of ethylene at 120 mA cm^{-2}. Furthermore, the $Cu^{\delta+}$NCN catalyst demonstrates outstanding durability, enabling continuous operation for nearly 80 h at a cell voltage of 3.6 V (Fig. 3h), thus exceeding the performance metrics of most catalysts documented to date (Supplementary Tab. 4).

Mechanism investigations

Studying the atomic structure-activity relationship of catalyst during the CO_2RR process is crucial to reveal the intrinsic catalytic mechanism. To assess the chemical state of Cu in the $Cu^{\delta+}$NCN under CO_2RR (Fig. 4a), *operando* XAS was performed (Supplementary Fig. 29), and the CuNCN was also measured for comparison (Fig. 4b). No obvious structural changes were observed from the XANES at open circuit potential (OCP) for both $Cu^{\delta+}$NCN and CuNCN (Fig. 4a, b). When the potential was elevated every 0.3 V from the potential range of −0.7 to −1.6 V vs. RHE, drastic change took place in the sample of CuNCN, suggesting a potential-dependent process. In contrast, the $Cu^{\delta+}$NCN displayed a slight change at the very beginning but negligible change with further increase of the applied potential. To make the comparison clearer, the variation of Cu valence state under the altered potential was plotted by comparing the first derivative energy position of the absorption edge (Fig. 4c, Supplementary Fig. 11). It could be clearly seen that at the initial potential of −0.7 V vs. RHE, the $Cu^{\delta+}$NCN still maintained the Cu oxidation state that close to the OCP condition. Above this potential, the valence state of Cu stayed stable between +0.2 and +0.5 and almost remained with an average valence state of about +0.3. Previous research also reported that the $[NCN]^{2-}$ group can safeguard the oxidation state of metals through a strong σ-donation effect and structural transformation, thereby maintaining the stability of the catalyst's average valence state[25]. In comparison, a gradual shift of the absorption edge to low energy side in the CuNCN was observed, accompanied by the formation of more deoxidized Cu ions (valence state :0.5 to 1.5). This irreversible Cu nanocluster formation would lead to leach of $[NCN]^{2-}$ group, which thus lead to the collapse of the open framework and loss of catalytic ability.

The changes of the atomic local structure around Cu in $Cu^{\delta+}$NCN during CO_2RR were detected by Wavelet transforms for the k^3-weighted Cu K-edge EXAFS (Fig. 4d) and FT-EXAFS (Fig. 4e)[36–38]. Similar to the FT-EXAFS signal collected on pristine sample, under open-circuit condition, FT-EXAFS data of $Cu^{\delta+}$NCN showed one strong peak located at ~ 1.5 Å and a weak peak at ~ 2.2 Å. Considering that the coordination of N, C, and O with Cu is difficult to be distinguished in EXAFS, for the sake of $Cu^{\delta+}$NCN structural determinism, we performed the fitting with these two peaks corresponding to the typical scattering features of the Cu-N/C/O and Cu-Cu coordination, respectively, and the fitted data match the experimental data very well (Supplementary

https://doi.org/10.1038/s41467-024-52022-0

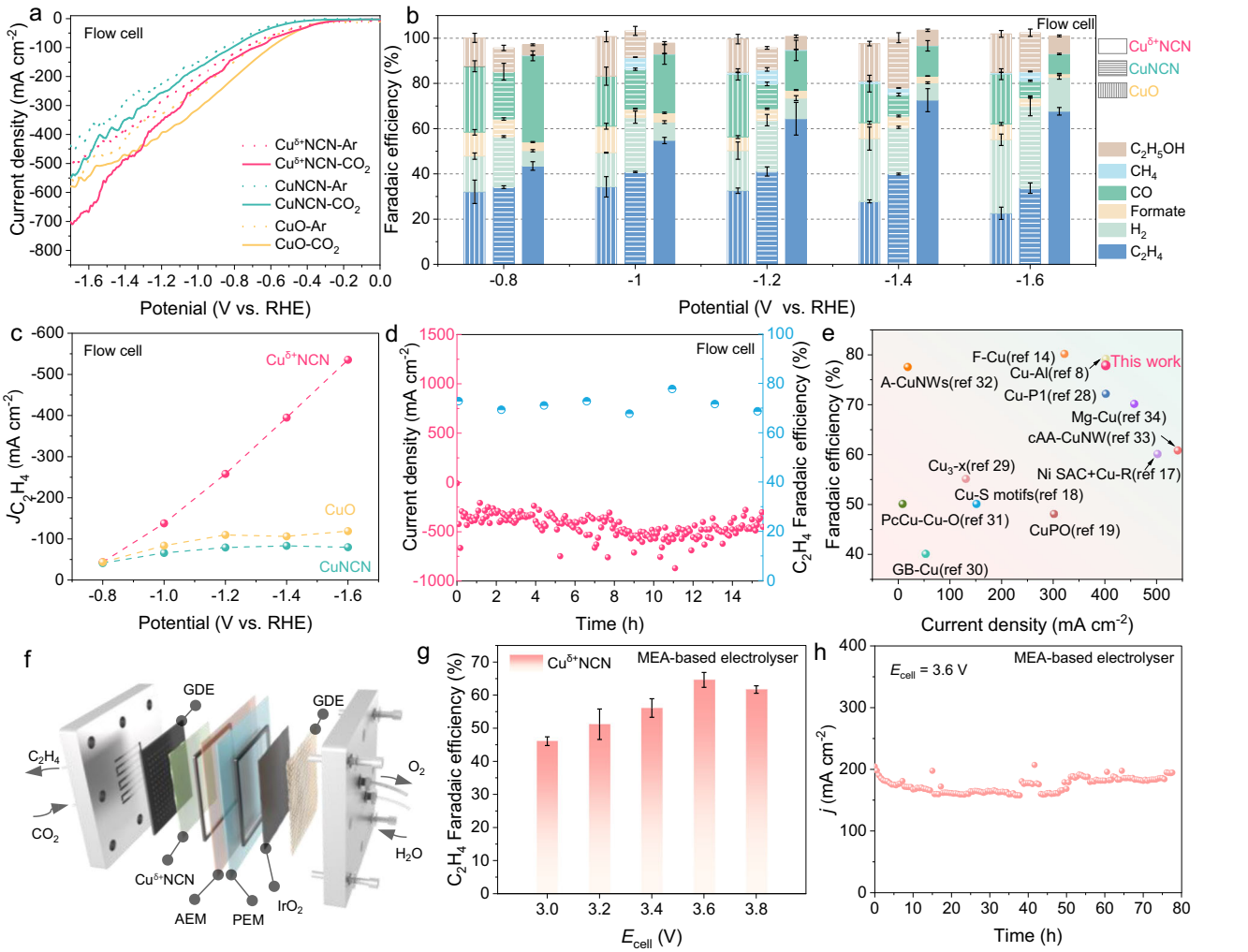

Fig. 3 | CO_2 electroreduction performances. a LSV curves of Cu$^{\delta+}$NCN, CuNCN and CuO in a flow cell under CO_2 or Ar atmospheres. **b** FE of various products from Cu$^{\delta+}$NCN, CuNCN and CuO at different potentials in a flow cell. **c** Ethylene partial current densities of Cu$^{\delta+}$NCN, CuNCN and CuO at various potentials in a flow cell. **d** Performance of Cu$^{\delta+}$NCN in a three-electrode flow cell to produce ethylene. **e** Comparison of the FE_{C2H4} and reduction current of Cu$^{\delta+}$NCN with recently reported catalysts. **f** Schematic illustration of the APMA-MEA biphasic electrode system apparatus. **g** FE_{C2H4} of Cu$^{\delta+}$NCN at various potentials in a biphasic electrode MEA system. **h** Stability performance of Cu$^{\delta+}$NCN within the MEA to produce ethylene.

Figs. 25, 26). When applying a potential of −0.7 V vs. RHE, the scattering peak for Cu-N/C/O bond was on a general downward trend along with the increasing of Cu–Cu bond intensity as the potential decreased (Fig. 4d, e). The conversion of CO_2-to-C_2H_4 reaction occurred simultaneously. Moreover, the intensity of bond pairs regarding Cu-N/C/O bond stabilized while the Cu–Cu bond slowly increased on subsequent potential decrease from −0.7 V to −1.3 V vs. RHE. In parallel, the FT-EXAFS fitting results of Cu$^{\delta+}$NCN showed that the coordination number of Cu-N/C/O in the first shell stayed relatively stable nearby 1.5 along with increase of CN for Cu–Cu from 0.5 to 1.0 (Fig. 4f, Supplementary Fig. 25&26 and Table S2). In contrast, the coordination number of Cu-N/C/O and Cu–Cu for CuNCN exhibited obvious decline, suggesting an irreversible Cu atom evolution from the $[NCN]^{2-}$ framework (Supplementary Figs. 12–14, Supplementary Figs. 27, 28 and Table S3). Note that at the potential range of −0.7 V to −1.3 V vs. RHE, Cu$^{\delta+}$NCN displayed stable and high FE_{C2H4} (> 50%) while FE $_{C2H4}$ on CuNCN decreased gradually concurrently. In particular, for Cu$^{\delta+}$NCN, the coordination number of Cu–Cu displayed a crude transfer to 1.6 once a larger negative voltage of −1.6 V vs. RHE was applied, which was accompanied by the appearance of a new Cu-N/C/O bond with coordination number of 1.4 and bond length 2.49 Å (Fig. 4g). Combined with the optimal activity intervals and the excellent stability of Cu$^{\delta+}$NCN in Fig. 3b, d, it can be judged that the coordination stability of Cu-N/C/O is crucial for Cu$^{\delta+}$NCN to maintain its catalytic stability[39]. And When the voltage is further increased to −1.6 V or higher in a flow cell, a significant decrease in the coordination number of Cu-N/C/O on the surface of Cu$^{\delta+}$NCN is observed. This is accompanied by a rapid increase in the coordination number of Cu-Cu, indicating that under the influence of voltage, in addition to the small amount of Cu clusters initially aggregated in a thermodynamically favorable manner, new Cu atoms have aggregated due to the breaking of some Cu-N/C/O bonds.

It is noteworthy that, at the same time, a new coordination attributed to Cu-N/C/O with a bond length of approximately 2.58 Å has emerged. This newly formed coordination will re-coordinate and stabilize these already formed Cu clusters, thereby ensuring the coexistence of Cu^0 and Cu^{1+} on the surface. The coexistence of Cu^0 and Cu^{1+} on the surface is highly consistent with the excellent stability of Cu$^{\delta+}$NCN during the CO_2RR process. We also investigated the physical phases as well as the surface chemical states of Cu$^{\delta+}$NCN and CuNCN after undergoing CO_2RR by XRD, XPS, SEM and EDS spectroscopy. Both XRD and SEM indicated that the phase and structure of Cu$^{\delta+}$NCN almost preserved, with only a small peak for metallic state Cu (~ 43.3°) observed (Supplementary Figs. 15, 16), in good agreement with the increased CN of Cu–Cu bond in *operando* XAS. In contrast, besides of

https://doi.org/10.1038/s41467-024-52022-0

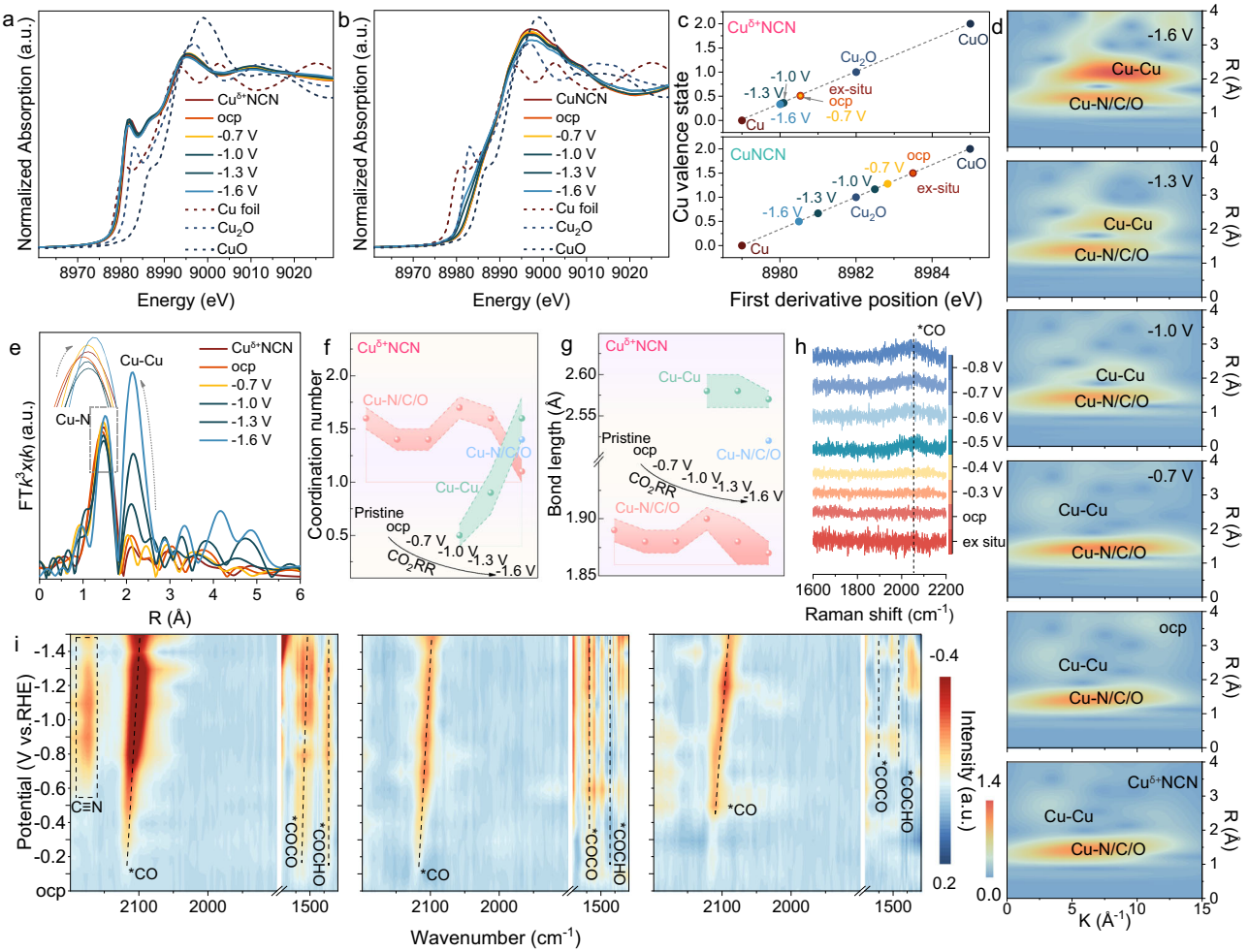

Fig. 4 | Mechanism investigations. *Operando* XANES spectra of **a** Cu$^{\delta+}$NCN and **b** CuNCN. **c** Fitted linear relationship between the energy position of the Cu K-edge in *operando* XANES spectra and the valence state of Cu. **d** Comparison of the EXAFS WTs of the Cu K-edge recorded during *operando* testing on Cu$^{\delta+}$NCN. **e** Fourier-transformed k^3-weighted EXAFS signals of the Cu K-edge recorded at different potentials on Cu$^{\delta+}$NCN. **f** Changes of coordination number for the Cu–N, Cu–Cu and Cu–N/C coordination shells. **g** Changes of bond length for the Cu–N, Cu–Cu and Cu–N/C coordination shells. **h** *Operando* Raman spectra of Cu$^{\delta+}$NCN. **i** *Operando* ATR-SEIRA spectra of Cu$^{\delta+}$NCN, CuNCN and CuO.

the huge morphology changes for CuNCN and CuO reference samples (Supplementary Fig. 16), the phase of CuNCN experienced the reduction to Cu_2O and then to metallic Cu, while the CuO almost totally transformed to the metallic Cu (Supplementary Fig. 15). This observation was also proved by the EDS and related mapping results, where no N element can be detected in CuNCN, suggesting the continuous reducing of Cu^+ from the $[NCN]^{2-}$ lead to the collapse of open framework (Supplementary Fig. 17), in accord with the decreased coordination number observed in XAS (Supplementary Fig. 13). The surface chemical states of Cu$^{\delta+}$NCN and CuNCN after undergoing CO_2RR for different times were further analyzed by XPS (Supplementary Fig. 18). The C-N coordination can be clearly observed on the surface of Cu$^{\delta+}$NCN, whereas for CuNCN, C-N is almost not observed on the surface due to the loss of the $[NCN]^{2-}$ moiety (Supplementary Fig. 18a, b), which agrees with the results of EDS. The valence changes of Cu observed from *operando* XAS are also confirmed from Cu 2*p* high-resolution XPS and Cu LMM spectra (Supplementary Fig. 18d, e). When experiencing CO_2RR for different reaction times, Cu reduction in CuNCN is clearly detected, whereas Cu$^{\delta+}$NCN can maintain its surface chemical state even after a long time of reaction thanks to the protection of the oxidation state of strong σ-donation effect and structure transformation of $[NCN]^{2-}$ [25]. The *operando* XAS together with post characterization study revealed an important phenomenon in our catalyst, that is the coexistence of stabilized Cu^0-Cu^{1+} dual sites by cyanamide framework under the reaction conditions and which can be stable maintained even during and after CO_2RR.

To probe the catalytic intermediates and mechanism of CO_2 reduction by Cu$^{\delta+}$NCN, *operando* electrochemical Raman (Fig. 4h) and attenuated total reflection-surface enhanced infrared absorption (ATR-SEIRA) (Fig. 4i, Supplementary Figs. 19, 20) experiments were conducted. As seen from the Raman spectra of Cu$^{\delta+}$NCN in Fig. 4h, the peaks between ~ 2100 and 2000 cm^{-1} attributed to the linearly bound *CO species were observed. The increased peak intensity and peak areas suggested a high *CO surface coverage and a strong *CO binding capability. As widely revealed by previous work, the promoted CO_2-to-C_{2+} efficiency basically depends on the coverage of surface *CO[40]. The high surface *CO would suppress HER and is vital for the subsequently C–C coupling, thereby enhancing the CO_2-to-C_2H_4 conversion[41]. These *CO signal bands were also detected in the *operando* ATR-SEIRA spectra around the 2100 cm^{-1} (Fig. 4i), and both the peak intensity and area for Cu$^{\delta+}$NCN increased much more obviously with the altered potentials compared to that of CuNCN and CuO. Simultaneously, it is readily observable that as the voltage increases, the adsorption of CO on the surface of Cu$^{\delta+}$NCN is also further enhanced. This is consistent with the observation in Fig. 4f that the coordination number of Cu-Cu continues to increase with the application of voltage. The presence of

Cu^0 accelerates the activation of CO_2 on the catalyst surface, ensuring that Cu^{1+} sites can better adsorb CO, thereby further promoting the coupling of *CO-*CO. In parallel, a distinctive peak shoulder around 1530 cm^{-1}corresponding to the *COCO intermediate via *CO dimerization was observed in $Cu^{\delta+}$NCN and increased accordingly with scanning to more negative potentials[42]. Simultaneously, a relatively weak character peak line for *COCHO (1440 cm^{-1}), intermediate of hydrogenation of *CO dimer, was detected[43]. In contrast, these vital signals for CuNCN were much weaker, and almost negligible on CuO, which were consistent with the distinctive trend of C_{2+} products formation rates on the three samples. Prominently, a shoulder peak around ~ 2150 cm^{-1} presented when the potential was decreased, which corresponds to the C≡N vibration of the $[N-C\equiv N]^{2-}$ moiety, taking responsibility for the electron transfer and stabilization of Cu^{1+}. And importantly, by keeping the reaction time at the constant potential −1.6 V vs. RHE for 12 min (Supplementary Fig. 20), the signal for C≡N vibration was almost maintained, further revealing the robust structure of $Cu^{\delta+}$NCN. As discussed above, the *operando* XAS study in conjunction with *operando* Raman and ATR-SEIRA analysis elucidated that the isolated Cu^0-Cu^{1+} dual sites stabilized by the cyanamide framework can enhance the coverage of surface *CO and facilitate the pathway of *CO dimerization to form *COCHO, thus improving the selectivity for C_2H_4 during CO_2RR.

DFT calculations

Theoretical investigations based on density functional theory (DFT) calculations were further adopted to gain insight into the CO_2RR mechanism on $Cu^{\delta+}$NCN. According to the fine structural analysis on pristine $Cu^{\delta+}$NCN (Fig. 2), atomic isolated Cu^0 coordinated by the Cu-N in the Cu_2NCN was confirmed. During the electrochemical reaction, the thermodynamically favorable aggregation of these Cu^0 lead to formation of few-atom Cu clusters, as observed by *operando* XAS (Fig. 4a–g). In light of this, a Cu_2NCN coordinated Cu^0-Cu^0 dual atoms model was used to represent the catalytic site to simplify the calculation (Supplementary Fig. 21). Considering that the Cu^0 atoms on the surface of Cu_2NCN might be influenced by the paramagnetic of Cu_2NCN, we also studied the effects of different spin states on the energy calculations prior to computing the energy of the Cu^0 sites. The results show that, in comparison with $M_{Cu} = 0$, higher spin of the Cu^0 atoms such as $M_{Cu} = 1$, 2, and 3 μB can significantly increase the total energies by 1.12 ~ 12.23 eV, indicating the $M_{Cu} = 0$ is the rational magnetic moment for Cu^0 atoms (Supplementary Fig. 22). The charge density difference was calculated for the surface copper and the second layer of copper using the Bader charge analysis method. Interestingly, the charge distribution between Cu atoms was charge-asymmetry as shown in Fig. 5a. The charge density of the Cu coordinated with the cyanamide (+0.77 e^-) was lower than that of the surface isolated metallic Cu atom (+0.83 e^-), proving the electron delocalization effect resulted from the $[NCN]^{2-}$. 3D charge density distribution model in Supplementary Fig. 23 further indicated the direct electron transfer from cyanamide framework in $Cu^{\delta+}$NCN to surface metallic Cu atom, leading to a significant electron accumulation at surface Cu^0 sites and substantial electron depletion at the Cu^{1+} sites, such electron distribution was vital for the stabilization of oxidized Cu^{1+} and the preserve of surface neutral Cu^0. We calculated the density of states projected on Cu^0, Cu^{1+}, and the coordinating N atoms. The intense charge transfer implies strong orbital hybridization and overlaps between the involved atoms, as shown below, the results show obvious hybridization and overlap between the Cu^0 3*d*, Cu^{1+} 3*d*, and N 2*p* orbitals,

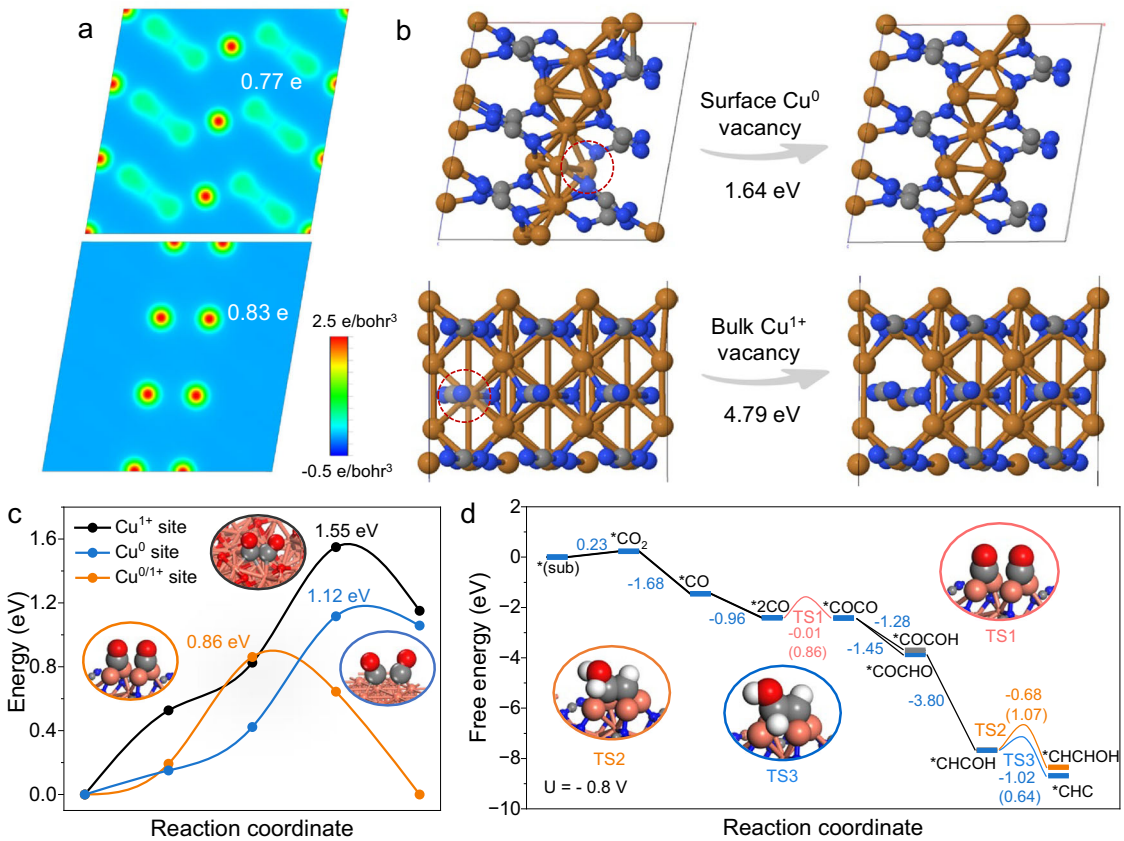

Fig. 5 | DFT calculations. a Charge density section plots of surface Cu atoms and second layer Cu atoms of $Cu^{\delta+}$NCN. **b** Vacancy formation energy of surface Cu^0 and bulk phase Cu^{1+}. **c** Energy barriers of *CO-*CO coupling on the $Cu^{\delta+}$NCN surface, Cu (111) surface, and Cu_2O (110) surface at U = −0.8 V. The corresponding transition state structures are shown in the insets. **d** Free energy profiles of the involved reaction intermediates under U = −0.8 V, the corresponding kinetic barriers of key reaction steps are provided in the brackets, the atomic structures of the transition states are shown in the insets.

which indicate strong bindings between Cu^0, Cu^{1+}, and the coordinating N atoms, leading to stabilized Cu^0 and Cu^{1+}. Meanwhile, for Cu^0 and $Cu1^+$ in the surface and bulk phases, we calculated the vacancy formation energies of bulk Cu^{1+} and surface Cu^0 in $Cu^{\delta+}$NCN, respectively, and the results, as shown in Fig. 5b, show that the vacancy formation energy of Cu^{1+} (4.79 eV), which is significantly higher than that of the surface Cu^0 (1.64 eV), which suggests that the bulk Cu^{1+} is more stable than the surface Cu^0. This result agreed well with the *operando* XAS observation, where the formation of few-atom Cu clusters was detected at high reduction potential, but still retained their native structure and demonstrate good stability due to the strong interaction of Cu-N with surface metallic Cu. We further investigated the dimerization kinetics of *CO to *OCCO on Cu surfaces with different oxidation states. As shown in Fig. 5c, when the catalyst surface is entirely composed of Cu^{1+}, the dimerization of *CO on the surface requires overcoming a high activation energy barrier (1.55 eV) to form the transient state (TS1). When the catalyst surface is entirely composed of Cu^0, the barrier for TS1 is reduced to 1.12 eV. However, on the surface of $Cu^{\delta+}$NCN (coexistence of Cu^0/Cu^{1+}), the barrier for TS1 is further reduced to 0.86 eV. This clearly demonstrates the importance of the Cu^0/Cu^{1+} environment maintained by CuNCN for the efficient production of C_2 products[44,45].

Mechanisms for the generation of C_2H_4 product have been widely explored and many different reaction pathways have been proposed[46,47]. The *CO mechanism was preferred for $Cu^{\delta+}$NCN than the *OCHO mechanisms due to the continuous generation of the CO product with the formation of C_2H_4 in the testing window as shown in Fig. 3b. By combing the results of *operando* ATR-SEIRA analysis (Fig. 4i), the hydrogenated *CO dimer (*COCHO) formed a key C_2 intermediate *CHCOH after a sequence of proton and electron transfer steps[48]. As a later key stage of the C_2 pathway, the hydrogenation of *CHCOH can lead to branching pathways to either ethylene or ethanol. On the basis of reaction free energies (ΔG) calculated at constant potential of −0.8 V in Fig. 5d, the *CHC pathway representing the formation of ethylene was proved to be more energetically favorable with a free energy change of -1.02 eV, much lower than that for *CHCHOH (ΔG = -0.68 eV), the typical pathway for ethanol. We further studied the kinetic barrier of this step, the barrier of *CHCOH → *CHCHOH is 1.07 eV, while the barrier of *CHCOH → *CHC is only 0.64 eV, indicating the formation of ethylene via *CHC intermediate is more favorable than the formation of ethanol in kinetics, consistent with our experimental results. Together, the reaction pathway of CO_2 to C_2H_4 on $Cu^{\delta+}$NCN was proposed as: CO_2 → *CO → *COCO → *COCHO → *CHCOH → *CHC → C_2H_4 based on the both *operando* characterization and theoretical calculations (Fig. 5d and Supplementary Tab. 5).

We have proposed a cyanamide coordinated isolated Cu framework with balanced metallic Cu (Cu^0) and delocalized Cu (Cu^{1+}) sites acts as an efficient electrocatalyst for CO_2-to-C_2H_4 reduction. These isolated neutral Cu^0 atoms in $Cu^{\delta+}$NCN enhanced the surface *CO by activating CO_2, while the electron delocalized Cu^{1+} lead to boost of C−C coupling by offering a lower reaction free energy for *CHC formation and high selectivity for C_2H_4. The tangible $Cu^{\delta+}$NCN catalyst exhibited one of the highest reported CO_2RR selectivity towards C_2H_4 with Faradaic efficiency of 77.7% at the partial current density of 400 mA cm^{-2}, togethering with stable reduction capability of CO_2-to-C_2H_4 for almost 80 h in a MEA-based electrolyser. Our work not only suggests an ingenious strategy to selective to stabilize the valence state of Cu to realize the product selectivity of CO_2RR, but it also introduces the specific coordination structures in designing CO_2RR materials for the electrosynthesis of high value-added products.

Methods

Chemicals

Copper chloride, copper nitrate, sodium hydroxide, cyanamide, Iridium (IV) Oxide and hydrazine were purchased from Adamas. Anion-exchange membrane (Fumasep-FAA-3-50) and anion-exchange membrane solution was purchased from Fumatech, German. Proton exchange membrane (N212) and Nafion perfluorinated resin (5 wt%) were purchased from DuPont, USA. All chemicals were used directly from the manufacturer without further purification.

Synthesis of $Cu^{\delta+}$NCN

The procedure for the fabrication of $Cu^{\delta+}$NCN was modified based on methodologies delineated in prior literature[24]. At room temperature, 426.6 mg of copper chloride was dissolved in 45 mL deionized water. Next, 2.5 mL of 3.5 M sodium hydroxide and 3 mL of 2 M cyanamide were added in order. The mixture was stirred for 3 minutes, then 5 mL of hydrazine was quickly poured in. After 2 h of reaction, the mixture was centrifuged, washed with deionized water, centrifuged again, and the final product was obtained by freeze-drying.

Synthesis of CuNCN

CuNCN was synthesized in a similar manner to $Cu^{\delta+}$NCN, except that hydrazine was not added during the synthesis.

Synthesis of CuO

This approach is in accordance with the methodologies delineated in prior studies[49]. Copper Oxide (CuO) were synthesized utilizing the hydrothermal technique, employing copper (II) nitrate ($Cu(NO_3)_2$) as the precursor. An aqueous sodium hydroxide solution with a molarity of three moles per liter (3 M, 2 mL) was incrementally introduced into a copper (II) nitrate solution of one mole per liter (1 M, 2 mL). The resultant mixture was subjected to vigorous stirring for a duration of one hour to ensure homogeneity. Subsequently, the mixture was subjected to a thermal treatment at a temperature of 120 °C for 4 h. Upon completion of the heating phase, the system was allowed to equilibrate to room temperature. The final stage encompassed a series of purification steps including centrifugation, meticulous washing, and a drying process.

Materials characterization

The surface textures and elemental distribution of the catalysts were meticulously delineated utilizing a field-emission scanning electron microscope (FE-SEM, Zeiss Gemini 300). The assessment of elemental composition and quantification was conducted through an Energy Dispersive X-ray Spectroscopy (EDS, JEOL-2010) apparatus integrally connected to the FE-SEM. Scanning transmission electron microscopy (STEM) images alongside energy-dispersive X-ray spectroscopy (EDS) mappings were procured using a JEOL ARM300 microscope. This state-of-the-art instrument boasts the capability of capturing ultrahigh-resolution STEM images with an exceptional spatial resolution of 63 picometers. The microscope is outfitted with a dual spherical aberration (CS) corrector, enhancing image clarity and precision. Additionally, it is equipped with an advanced X-ray energy dispersive spectrometer (JED-2300 Series), which incorporates a pair of 158 mm^2 solid-state detectors (SSD) for superior spectral sensitivity and precise elemental analysis. To decipher the crystalline architecture of the samples, X-ray diffraction (XRD) profiles were acquired using a Bruker D8-Advance X-ray diffractometer, employing Cu-*Kα* radiation. The catalyst samples were aerated and methodically surveyed across a range of 5 to 80 degrees at a rate of 5 degrees per minute. The KPFM characterization was carried out with atomic force microscope (nanoIR2-FS). Inductively coupled plasma atomic emission spectroscopy (ICP-OES) was performed on an Agilent 5110 ICP spectrometer. Analysis of the valence states of the elemental constituents was executed via X-ray photoelectron spectroscopy (XPS, Thermo Scientific K-Alpha). Prior to engaging in curve fitting and background attenuation, a standardization of the XPS spectra was performed referencing the C 1*s* peak. The Fourier-transform infrared (FTIR) spectra were captured

using a Thermo Scientific Nicolet iS20 spectrophotometer; each sample was meticulously prepared by compressing it into a pellet with KBr powder.

Electrochemical measurement

The assessment of CO_2 reduction reaction (CO_2RR) efficacy was meticulously conducted within both a flow cell and a membrane electrode assembly (MEA) electrolytic cell. apparatus.

Within the flow cell measurements, an electrolytic solution of 1 M KOH, exhibiting a pH of 13.8, was utilized as both the anolyte and catholyte. The gaseous environments perfusing the cathodic compartment were composed of CO_2 and Argon, tailored to the specific exigencies of the reaction conditions. The trifecta of electrodes comprised a gas-diffusion layer measuring 1 cm by 3 cm, a platinum sheet of identical dimensions, and a silver/silver chloride (Ag/AgCl) reference electrode immersed in saturated KCl, each meticulously arranged, with the active operative surface area precisely defined at 1 cm^2. The catalyst loading on the cathode is 0.7 mg cm^{-2}. An anion exchange membrane of type FAA-3-50 provided a discrete partition between the cathode and anode chambers. The regulation of gaseous flow was achieved with a mass flowmeter, maintaining a rate of 40 mL min^{-1}, while a peristaltic pump assiduously controlled the electrolyte flow at a rate of 10 mL min^{-1}. The calibration of potentialities was scrupulously performed in reference to the reversible hydrogen electrode (RHE), utilizing the equation: E (vs. RHE) = E (vs Ag/AgCl) + 0.197 V + (0.0592 × pH). Linear sweep voltammetry (LSV) was executed within the gas diffusion cell at a scanning velocity of 10 mV s^{-1}, traversing a potential range from 0 to −1.7 V versus RHE. The electrochemical active surface area (ECSA) of the catalyst was appraised by gauging electrochemical capacitance over scanning velocities ranging from 20 to 100 mV s^{-1}, with increments of 20 mV s^{-1}, within a non-Faradaic potential window. The electrochemical double-layer capacitance (C_{dl}) of the specimen was estimated by the differential current (Δj) at the varying scanning rates. All voltages were not subjected to *iR* compensation.

Within the MEA electrolytic cell measurements, using a homemade flow channel plate as a jig, a Nafion N212 membrane as the PEM, and Fumasep-FAA-3-50 as the AEM, an APMA-MEA system was constructed. The anode catalyst employed was iridium dioxide with a loading of 2 mg cm^{-2}, which was applied to the pre-treated PEM through the CCM (Catalyst Coated Membrane) method and thermally pressed before use. The anode gas diffusion layer utilized a platinum-coated titanium mesh. The cathode catalyst was $Cu^{6+}NCN$ with a loading of 2 mg cm^{-2}, which was spray-coated onto YLS-30T carbon paper using the CCS (Catalyst Coated Substrate) method and was not thermally pressed. The anolyte is deionized water with a flow rate controlled at 30 milliliters per minute, while the cathode gas is humidified with deionized water at 50 °C before entering the cathode chamber, with its flow rate controlled at 30 standard cubic centimeters per minute (sccm). The MEA testing is performed using chronoamperometry. All electrochemical tests were conducted at room temperature.

Products analysis

The electrochemical reduction of CO_2 was meticulously conducted at ambient temperature, employing a saturated 1 M KOH electrolytic solution across a potential range of −0.8 V to −1.6 V with respect to the reversible hydrogen electrode (RHE). The cathodic electrolysis was methodically sustained for a duration of 20 minutes at each discrete potential setting. Concurrently, oxygen evolution at the anode was expelled along with the electrolyte via the methodical action of a peristaltic pump. The identification and quantification of gaseous byproducts emanating from the cathodic domain of the electrocatalytic CO_2 reduction were assiduously monitored through online gas chromatography equipped with both a flame ionization detector (FID) and a thermal conductivity detector (TCD) (Model A91 Plus, Panna Instruments, China), with analyses conducted at five-minute intervals.

Throughout the CO_2 reduction reaction, the gaseous outputs from both the flow cell and the MEA electrolytic cell were quantitatively ascertained via online chromatographic analysis on a bi-temporal basis of five minutes, utilizing the dual-detection system.

The faradaic efficiency (FE) of the gaseous products was calculated using the equation:

$$FE(\%) = \frac{Q_{products}}{Q_{total}} \times 100\% = \frac{\upsilon \times x \times N \times F}{j} \times 100\% \quad (1)$$

where (υ) denotes the volumetric flow of CO_2 through the cathodic chamber (volume per second), (x) represents the product concentration as determined from a 1 ml sample loop calibrated against a standard gas via online GC, (N) is the number of electrons transferred in the reduction process, (F) signifies the Faraday constant (96,485 C mol^{-1}), and (j) is the current density at the given moment.

Post-electrolysis, the cathodic liquid was diligently collected and subjected to a 400 MHz nuclear magnetic resonance (NMR) spectrometer for quantitation of the aqueous products. Following a 20-minute CO_2RR session at the specified potential, the electrolyte was gathered, and a 500 µL aliquot was mixed with 100 µL of a 10 mM DMSO solution and 100 µL of D_2O for diagnostic analysis of the liquid product profile via a 400 MHz ^{1}H-NMR spectrometer. To construct calibration curves, a series of liquid-phase products standards in DMSO and D_2O were assayed using NMR. Within the one-dimensional ^{1}H NMR spectra, the water signal was attentively suppressed, placing the DMSO and liquid-phase products proton resonances, respectively. The liquid-phase products concentration within the electrolyte was deduced from the standard curve.

Faradaic efficiency of the liquid-phase products was determined by the equation:

$$FE(\%) = \frac{Q_{\text{liquid-phase products}}}{Q_{total}} \times 100\% = \frac{V \times x \times N \times F}{\int_0^t j dt} \times 100\% \quad (2)$$

where (V) is the volume of the cathode electrolyte, (x) is the concentration of liquid-phase products, (N) is the number of electrons involved in the reduction process, (F) is the Faraday constant (96,485 C mol^{-1}), and (Q_{total}) is calculated by integrating the current over time.

Operando Raman spectroscopy

Operando Raman spectroscopy analyses were performed using a Horiba LabRAM HR Evolution system. The experimental arrangement for the electrode mirrored that of the antecedent electrochemical tests, with the modification of the electrolyte to a 0.1 M $KHCO_3$ solution. This modification was intended to mitigate the absorption of CO_2 by KOH. Spectral acquisition was performed under 532 nm laser excitation, operated at 10% of the laser potential intensity, and the exposure duration was set to 20 s. Open circuit voltage Raman spectra is the spectra collected by the sample directly immersed in 0.1 M $KHCO_3$. *Operando* Raman spectra were collected using chronoamperometry at −0.3 - −0.8 V vs. RHE without *iR* drop compensation.

Operando ATR-SEIRA spectroscopy

The catalytic layer was applied onto a chemically prepared Au film situated atop a Si ATR prism, with subsequent ATR-SEIRAS assessments conducted using a PerkinElmer Spectrum FTIR spectrometer,

integrated with a MCT detector. A spectral resolution of 4 cm^{-1} was selected. Spectral acquisition was conducted within the wavenumber range of 400 to 4000 cm^{-1}, with the number of scans set to four. During the testing process, Au film was utilized as the working electrode onto which the ink was drop-cast and dried prior to testing. A platinum slice served as the counter electrode, and Ag/AgCl electrode was used as the reference in a three-electrode setup. Electrolyte 0.5 M $KHCO_3$ was employed for the electrochemical measurements. Chronoamperometry was the technique used for the electrochemical test, with the test voltage range spanning from −0.1 V to −1.5 V vs. RHE. Spectral data were collected twice after a reaction time of 30 s at each potential. Finally, spectral data were continuously acquired for 12 min at a potential of −1.6 V vs. RHE.

Operando XAFS

The Cu K-edge XAFS spectra were measured at BL17B1 beamline of Shanghai Synchrotron Radiation Facility (SSRF), China. The storage ring of the SSRF were operated at 2.5 GeV with a maximum electron current of 250 mA. Operando XAFS measurements were performed in a homemade cell (Supplementary Fig. 29). Catalyst-loaded carbon paper as working electrode with polyimide film on the back side and then glued to the surface of the operando electrolytic cell, with the catalyst in direct contact with the electrolyte. A 0.5 M $KHCO_3$ solution was used as the electrolyte. All X-ray was monochromatized by a Si (111) double-crystal monochromator with the energy calibrated using Cu foils.

XAFS analysis and results

The acquired EXAFS data were processed according to the standard procedures using the ATHENA module of Demeter software packages[50].

The EXAFS spectra were processed by first removing the post-edge background from the total absorption and then normalizing it relative to the edge-jump step. Afterward, the χ(k) data were Fourier transformed into real (R) space using a Hanning window with a width of dk = 1.0 $Å^{-1}$ to distinguish the EXAFS contributions from various coordination shells. To extract the quantitative structural parameters surrounding the central atoms, least-squares curve fitting was carried out using the ARTEMIS module within the Demeter software suite[50].

The following EXAFS equation was used[51]

$$\chi(k) = \sum_j \frac{N_j S_0^2 F_j(k)}{kR_j^2} \cdot \exp\left[-2k^2\sigma_j^2\right] \cdot \exp\left[\frac{-2R_j}{\lambda(k)}\right] \cdot \sin\left[2kR_j + \phi_j(k)\right] \quad (3)$$

the theoretical calculations included scattering amplitudes, phase shifts, and photoelectron mean free paths for all considered paths. The amplitude reduction factor is represented by S_0^2, while $F_j(k)$ denotes the effective curved-wave backscattering amplitude. N_j represents the number of neighboring atoms in the j^{th} atomic shell, and R_j is the distance between the X-ray absorbing central atom and the atoms in the j^{th} atomic shell. The mean free path, denoted as λ, is expressed in Å. The phase shift, $\phi_j(k)$, encompasses both the individual shell phase shifts and the total phase shift for the central atom. The Debye-Waller factor, σ_j, characterizes the variation in distances around the average R_j within the j^{th} shell. The functions $F_j(k)$, λ, and $\phi_j(k)$ were computed using the ab initio software FEFF9. Further details on the EXAFS simulations are provided below.

All fits were performed in the *R* space with *k*-weight of 3 while phase correction was also applied in the first coordination shell to make R value close to the physical interatomic distance between the absorber and shell scatterer. The coordination numbers of model samples were fixed as the nominal values. The obtained S_0^2 was fixed in the subsequent fitting. While the internal atomic distances R, Debye-Waller factor σ^2, and the edge-energy shift Δ were allowed to run freely. The detailed analysis results are illustrated in Supplementary Tables 2, 3.

For Wavelet Transform analysis, the χ(k) exported from Athena was imported into the Hama Fortran code. The parameters were listed as follow: R range, 1–4 Å, k range, 0–15 $Å^{-1}$ for samples; k weight, 3; and Morlet function with κ = 10, σ = 1 was used as the mother wavelet to provide the overall distribution.

Density functional theory computation

Density functional theory (DFT) investigations were carried out using the Vienna ab initio simulation package (VASP). The interaction between ions and electrons under the frozen-core approximation was described employing the projector augmented wave (PAW) method[52]. Kohn-Sham valence states were expanded in a plane-wave basis set with a cut-off energy of 450 eV. Spin-polarized calculations utilized the Perdew-Burke-Ernzerhof (PBE) exchange-correlation functional within the generalized gradient approximation (GGA)[53,54]. The Brillouin zone integration employed a Monkhorst-Pack mesh of 3 × 3 × 1. To separate periodic images, a 15 Å vacuum was added. The atomic structures were relaxed until the forces were less than 0.03 eV $Å^{-1}$. For the implicit solution model, VASPsol was implemented to balance the net electronic charges introduced by the constant-potential method[55]. The relative permittivity was set to 78.4, and a linearized Poisson–Boltzmann model with a Debye length of 3.0 Å was employed to mimic the compensating charge. In addition, we obtained the charge values using the Bader charge analysis method.

Constant-potential method for obtaining the potential-dependent grand canonical energies. In the constant-potential calculations, the structures and work functions of the involved reaction intermediates were fully optimized to account for the effect of an applied potential. The optimization method we utilized is developed by Duan et al.[56]. The work functions of the reaction intermediates are related to the applied potential by referencing them to $\Phi_{SHE} = -4.6$ eV, which is the work function of the standard hydrogen electrode (SHE).

Free energy calculation method under constant potentials. In this work, the grand free energy changes (ΔG) of the key CO_2RR steps under a constant potential (U) were evaluated by Eq. (4):

$$\Delta G = \Delta E(U) + \Delta ZPE + \Delta G_U^{PCET} + \Delta G_{pH} + \Delta \int_0^T C_P dT - T\Delta S \quad (4)$$

where ΔZPE is the zero-point energy change, ΔG_U^{PCET} is the free energy contribution of proton-coupled electron transfer (PCET) at electrode potential U. $\Delta G_{pH} = 2.303 \times k_B T \times pH$ (or $0.06 \times pH$) eV. The entropy change is denoted as ΔS, while C_p signifies the constant-pressure heat capacity. The entropy and the integration term are obtained through the vibrational energy calculations of the CO_2RR intermediates.

In the above equation, E(U) is defined as a grand canonical energy of the system:

$$E(U) = E_{DFT} + \Delta n^{CPS} \cdot \left(U - V_{sol} + \frac{\Phi_{SHE}}{e}\right) \quad (5)$$

where E_{DFT} is the energy calculated from DFT, Δn^{CPS} is the number of electrons added or removed from the system, which is determined by the constant-potential method. Φ_{SHE} is the work function of the standard hydrogen electrode, SHE (−4.6 eV), and V_{sol} is the potential deep in the solution.

Formation energy of a Cu vacancy. The surface Cu^0 and bulk phase Cu^{1+} vacancy formation energies are defined as:

$$E_{vf} = E_{vac} + E_{Cu} - E_{tot} \quad (6)$$

where E_{vac} is total energy of the structure with a Cu vacancy, E_{Cu} is the energy of a single Cu atom, E_{tot} is the total energy of the pristine structure without any defects. In this work the energy of single Cu atom refers to an isolated Cu atom in vacuum.

Data availability

The data generated in this study are provided in the Supplementary Information and are available from the authors upon request. Source data are provided with this paper.

References

1. Fang, W. et al. Durable CO_2 conversion in the proton-exchange membrane system. *Nature* **626**, 86–91 (2024).
2. Wang, J. et al. Spatially and temporally understanding dynamic solid-electrolyte interfaces in carbon dioxide electroreduction. *Chem. Soc. Rev.* **52**, 5013–5050 (2023).
3. Woldu, A. R., Huang, Z., Zhao, P., Hu, L. & Astruc, D. Electrochemical CO_2 reduction (CO_2RR) to multi-carbon products over copper-based catalysts. *Coord. Chem. Rev.* **454**, 214340 (2022).
4. Zhang, H., Gao, J., Raciti, D. & Hall, A. S. Promoting Cu-catalysed CO_2 electroreduction to multicarbon products by tuning the activity of H_2O. *Nat. Catal.* **6**, 807–817 (2023).
5. Chen, Y. et al. Efficient multicarbon formation in acidic CO_2 reduction via tandem electrocatalysis. *Nat. Nanotechnol.* **19**, 311–318 (2023).
6. Fang, W. et al. Low-coordination Nanocrystalline Copper-based Catalysts through Theory-guided Electrochemical Restructuring for Selective CO_2 Reduction to Ethylene. *Angew. Chem. Int. Ed.* **63**, e202319936 (2024).
7. Huang, J. E. et al. CO_2 electrolysis to multicarbon products in strong acid. *Science* **372**, 1074–1078 (2021).
8. Zhong, M. et al. Accelerated discovery of CO_2 electrocatalysts using active machine learning. *Nature* **581**, 178–183 (2020).
9. Amirbeigiarab, R. et al. Atomic-scale surface restructuring of copper electrodes under CO_2 electroreduction conditions. *Nat. Catal.* **6**, 837–846 (2023).
10. Gao, W., Xu, Y., Fu, L., Chang, X. & Xu, B. Experimental evidence of distinct sites for CO_2-to-CO and CO conversion on Cu in the electrochemical CO_2 reduction reaction. *Nat. Catal.* **6**, 885–894 (2023).
11. Wang, X. et al. Morphology and mechanism of highly selective Cu (II) oxide nanosheet catalysts for carbon dioxide electroreduction. *Nat. Commun.* **12**, 794 (2021).
12. De Luna, P. et al. Catalyst electro-redeposition controls morphology and oxidation state for selective carbon dioxide reduction. *Nat. Catal.* **1**, 103–110 (2018).
13. Wang, J. et al. Strong Correlation between the Dynamic Chemical State and Product Profile of Carbon Dioxide Electroreduction. *ACS Appl. Mater. Interfaces* **14**, 22681–22696 (2022).
14. Ma, W. et al. Electrocatalytic reduction of CO_2 to ethylene and ethanol through hydrogen-assisted C–C coupling over fluorine-modified copper. *Nat. Catal.* **3**, 478–487 (2020).
15. Feng, J. et al. Improving CO_2-to-C_{2+} Product Electroreduction Efficiency via Atomic Lanthanide Dopant-Induced Tensile-Strained CuO_x Catalysts. *J. Am. Chem. Soc.* **145**, 9857–9866 (2023).
16. Wang, J., Tan, H. Y., Zhu, Y., Chu, H. & Chen, H. M. Linking the Dynamic Chemical State of Catalysts with the Product Profile of Electrocatalytic CO_2 Reduction. *Angew. Chem. Int. Ed.* **60**, 17254–17267 (2021).
17. Liu, M. et al. Potential Alignment in Tandem Catalysts Enhances CO_2-to-C_2H_4 Conversion Efficiencies. *J. Am. Chem. Soc.* **146**, 468–475 (2024).
18. Wen, C. F. et al. Highly Ethylene-Selective Electrocatalytic CO_2 Reduction Enabled by Isolated Cu- S Motifs in Metal–Organic Framework Based Precatalysts. *Angew. Chem. Int. Ed.* **61**, e202111700 (2022).
19. Zhang, X. Y. et al. Direct OC-CHO coupling towards highly C_{2+} products selective electroreduction over stable Cu^0/Cu^{2+} interface. *Nat. Commun.* **14**, 7681 (2023).
20. Lin, S.-C. et al. Operando time-resolved X-ray absorption spectroscopy reveals the chemical nature enabling highly selective CO_2 reduction. *Nat. Commun.* **11**, 3525 (2020).
21. Su, X. et al. Complementary operando spectroscopy identification of in-situ generated metastable charge-asymmetry Cu_2-CuN_3 clusters for CO_2 reduction to ethanol. *Nat. Commun.* **13**, 1322 (2022).
22. Xu, H. et al. Highly selective electrocatalytic CO_2 reduction to ethanol by metallic clusters dynamically formed from atomically dispersed copper. *Nat. Energy* **5**, 623–632 (2020).
23. Jia, B., Sun, D., Zhao, W. & Huang, F. Metal cyanamides: Open-framework structure and energy conversion/storage applications. *J. Energy Chem.* **61**, 347–367 (2021).
24. Kong, S. et al. Delocalization state-induced selective bond breaking for efficient methanol electrosynthesis from CO_2. *Nat. Catal.* **6**, 6–15 (2023).
25. Jia, B. et al. Indium Cyanamide for Industrial-Grade CO_2 Electroreduction to Formic Acid. *J. Am. Chem. Soc.* **145**, 14101–14111 (2023).
26. Wang, J. et al. In situ X-ray spectroscopies beyond conventional X-ray absorption spectroscopy on deciphering dynamic configuration of electrocatalysts. *Nat. Commun.* **14**, 6576 (2023).
27. Wu, Z.-Z. et al. Identification of Cu (100)/Cu (111) interfaces as superior active sites for CO dimerization during CO_2 electroreduction. *J. Am. Chem. Soc.* **144**, 259–269 (2021).
28. Chen, X. et al. Electrochemical CO_2-to-ethylene conversion on polyamine-incorporated Cu electrodes. *Nat. Catal.* **4**, 20–27 (2021).
29. Lu, Y. F. et al. Predesign of catalytically active sites via stable coordination cluster model system for electroreduction of CO_2 to ethylene. *Angew. Chem. Int. Ed.* **60**, 26210–26217 (2021).
30. Chen, Z. et al. Grain-boundary-rich copper for efficient solar-driven electrochemical CO_2 reduction to ethylene and ethanol. *J. Am. Chem. Soc.* **142**, 6878–6883 (2020).
31. Qiu, X.-F., Zhu, H.-L., Huang, J.-R., Liao, P.-Q. & Chen, X.-M. Highly selective CO_2 electroreduction to C_2H_4 using a metal–organic framework with dual active sites. *J. Am. Chem. Soc.* **143**, 7242–7246 (2021).
32. Choi, C. et al. Highly active and stable stepped Cu surface for enhanced electrochemical CO_2 reduction to C_2H_4. *Nat. Catal.* **3**, 804–812 (2020).
33. Kim, J. et al. Vitamin C-induced CO_2 capture enables high-rate ethylene production in CO_2 electroreduction. *Nat. Commun.* **15**, 192 (2024).
34. Xie, M. et al. Fast Screening for Copper-Based Bimetallic Electrocatalysts: Efficient Electrocatalytic Reduction of CO_2 to C_{2+} Products on Magnesium-Modified Copper. *Angew. Chem. Int. Ed.* **61**, e202213423 (2022).
35. She, X. et al. Pure-water-fed, electrocatalytic CO_2 reduction to ethylene beyond 1,000 h stability at 10 A. *Nat. Energy* **9**, 81–91 (2024).
36. Chang, C. J. et al. Dynamic Reoxidation/Reduction-Driven Atomic Interdiffusion for Highly Selective CO_2 Reduction toward Methane. *J. Am. Chem. Soc.* **142**, 12119–12132 (2020).
37. Hsu, C.-S. et al. Activating dynamic atomic-configuration for single-site electrocatalyst in electrochemical CO_2 reduction. *Nat. Commun.* **14**, 5245 (2023).
38. Tan, H. Y. et al. Reversibly Adapting Configuration in Atomic Catalysts Enables Efficient Oxygen Electroreduction. *J. Am. Chem. Soc.* **145**, 27054–27066 (2023).
39. Yang, D., Zuo, S., Yang, H., Zhou, Y. & Wang, X. Freestanding millimeter-scale porphyrin-based monoatomic layers with 0.28 nm thickness for CO_2 electrocatalysis. *Angew. Chem. Int. Ed.* **59**, 18954–18959 (2020).

40. Wang, X. et al. Mechanistic reaction pathways of enhanced ethylene yields during electroreduction of CO_2–CO co-feeds on Cu and Cu-tandem electrocatalysts. *Nat. Nanotechnol.* **14**, 1063–1070 (2019).
41. Li, J. et al. Enhanced multi-carbon alcohol electroproduction from CO via modulated hydrogen adsorption. *Nat. Commun.* **11**, 3685 (2020).
42. Kim, Y. et al. Time-resolved observation of C–C coupling intermediates on Cu electrodes for selective electrochemical CO_2 reduction. *Energy Environ. Sci.* **13**, 4301–4311 (2020).
43. Delmo, E. P. et al. In Situ Infrared Spectroscopic Evidence of Enhanced Electrochemical CO_2 Reduction and C-C Coupling on Oxide-Derived Copper. *J. Am. Chem. Soc.* **146**, 1935–1945 (2024).
44. Zhang, J. et al. Grain Boundary-Derived Cu^+ /Cu^0 Interfaces in CuO Nanosheets for Low Overpotential Carbon Dioxide Electroreduction to Ethylene. *Adv. Sci.* **9**, e2200454 (2022).
45. Yuan, X. et al. Controllable Cu^0 -Cu^+ Sites for Electrocatalytic Reduction of Carbon Dioxide. *Angew. Chem. Int. Ed.* **60**, 15344–15347 (2021).
46. Kastlunger, G., Heenen, H. H. & Govindarajan, N. Combining First-Principles Kinetics and Experimental Data to Establish Guidelines for Product Selectivity in Electrochemical CO_2 Reduction. *ACS Catal.* **13**, 5062–5072 (2023).
47. Li, X., Wu, X., Lv, X., Wang, J. & Wu, H. B. Recent advances in metal-based electrocatalysts with hetero-interfaces for CO_2 reduction reaction. *Chem. Catal.* **2**, 262–291 (2022).
48. Li, Y. C. et al. Binding Site Diversity Promotes CO_2 Electroreduction to Ethanol. *J. Am. Chem. Soc.* **141**, 8584–8591 (2019).
49. Wang, P. et al. Sub-1 nm Cu_2O Nanosheets for the Electrochemical CO_2 Reduction and Valence State–Activity Relationship. *J. Am. Chem. Soc.* **145**, 26133–26143 (2023).
50. Ravel, B. & Newville, M. ATHENA, ARTEMIS, HEPHAESTUS: data analysis for X-ray absorption spectroscopy using IFEFFIT. *J. Synchrotron Radiat.* **12**, 537–541 (2005).
51. Newville, M. EXAFS analysis using FEFF and FEFFIT. *J. Synchrotron Radiat.* **8**, 96–100 (2001).
52. Blöchl, P. E. Projector augmented-wave method. *Phys. Rev. B* **50**, 17953 (1994).
53. Perdew, J. P., Burke, K. & Ernzerhof, M. Generalized gradient approximation made simple. *Phys. Rev. Lett.* **77**, 3865 (1996).
54. Hammer, B., Hansen, L. B. & Nørskov, J. K. Improved adsorption energetics within density-functional theory using revised Perdew-Burke-Ernzerhof functionals. *Phys. Rev. B* **59**, 7413–7421 (1999).
55. Mathew, K., Kolluru, V. S. C., Mula, S., Steinmann, S. N. & Hennig, R. G. Implicit self-consistent electrolyte model in plane-wave density-functional theory. *J. Chem. Phys.* **151**, 234101 (2019).
56. Duan, Z. & Xiao, P. Simulation of Potential-Dependent Activation Energies in Electrocatalysis: Mechanism of O–O Bond Formation on RuO_2. *J. Phys. Chem. C.* **125**, 15243–15250 (2021).

Acknowledgements

This project is funded by financial support from the National Natural Science Foundation of China (22279159, YY), Natural Science Foundation of Shanghai (22ZR1471900, YY) and Shanghai Rising-Star Program (22QA1410300, YY). We also thank BL17B1 and BL 20U station at Shanghai Synchrotron Radiation Facility (SSRF) for the help in characterizations and supercomputing Facilities were provided by Hefei Advanced Computing Center.

Author contributions

Y.Y. and F.Q.H. conceived the idea of the project. K.H.Y., H.H.H. and Y.Y. designed and carried out the electrochemical experiments, Y.Y.Q. carried out the DFT calculations, Y.Q.S. and Y.Y. supervised and advised the DFT calculations, K.H.Y. and Y.Y. performed and discussed XAS characterization, Z.R.L. and M.Z.C. contributed to result discussion and data analysis, F.Q.H. commented and revised the manuscript. Y.Y. and K.H.Y. wrote and revised the manuscript. All the authors discussed the results and assisted with the manuscript preparation.

Competing interests

The authors declare no competing interests.

Additional information

Supplementary information The online version contains supplementary material available at https://doi.org/10.1038/s41467-024-52022-0.

Correspondence and requests for materials should be addressed to Yaqiong Su, Fuqiang Huang or Ya Yan.

Peer review information *Nature Communications* thanks Biaobiao Zhang, Sze-Chun Tsang and the other, anonymous, reviewers for their contribution to the peer review of this work. A peer review file is available.